ACS APPLIED ENERGY MATERIALS

www.acsaem.org Article

Tuning the Nanoporous Structure of Carbons Derived from the Composite of Cross-Linked Polymers for Charge Storage Applications

Farshad Barzegar,* Vladimir Pavlenko, Muhammad Zahid, Abdulhakeem Bello, Xiaohua Xia, Ncholu Manyala, Kenneth I. Ozoemena, and Qamar Abbas*

Cite This: *ACS Appl. Energy Mater.* 2021, 4, 1763−1773 Read Online

ACCESS | Metrics & More | Article Recommendations | Supporting Information

ABSTRACT: Controlling the porosity of carbon-based electrodes is key toward performance improvement of charge storage devices, e.g., supercapacitors, which deliver high power via fast charge/discharge of ions at the electrical double layer (EDL). Here, eco-friendly preparation of carbons with adaptable nanopores from polymers obtained via microwave-assisted cross-linking of poly(vinyl alcohol) (PVA) and poly(vinyl pyrrolidone) (PVP) is reported. The polymeric hydrogels possess porous and foam-like structures, giving excellent control of porosity at the precursor level, which are then subjected to activation at high temperatures of 700−900 °C to prepare carbons with a surface area of 1846 m^2 g^{-1} and uniform distribution of micro-, meso-, and macropores. Then, graphene as an additive to hydrogel precursor improves the surface characteristics and elaborates porous texture, giving composite materials with a surface area of 3107 m^2 g^{-1}. These carbons show an interconnected porous structure and bimodal pore size distribution suitable for facile ionic transport. When implemented in symmetric supercapacitor configuration with aqueous 5 mol L^{-1} $NaNO_3$ electrolyte, a capacitance of 163 F g^{-1} (per average mass of one electrode) and stable evolution of capacitance, coulombic, and energy efficiency during 10 000 galvanostatic charge/discharge up to 1.6 V at 1.0 A g^{-1} have been achieved.

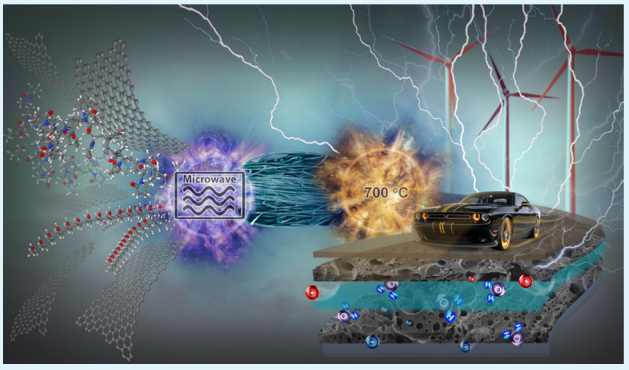

KEYWORDS: *microwave-assisted cross-linked polymers, nanoporous carbon, charge storage, electric double layer, supercapacitor*

INTRODUCTION

To meet the increasing energy demand of the modern world and to fill the niches requiring fast energy delivery and its simultaneous quick recovery,[1−5] new materials and methods are desirable. Carbon materials make up to 90 wt % of the electrode composition used in capacitive charge storage technologies such as supercapacitors, which are attractive devices for capturing energy from regenerative braking in tramways or in a start−stop system for automobiles.[6−8] Commercial carbons are mainly derived from biomass sources with predefined natural structure,[9−11] thus restricting the control over efficient storing and releasing of charges and hence their viability in an ever-growing energy sector. New methods and materials for designing carbons with optimized and compatible pore structure that can be tuned per application are therefore highly desirable. Since the fast charging/discharging of electric double layer (EDL) depends on the respective size of ions and pores,[12] this compatibility is at the heart of high-power and long-term cycling of supercapacitors.

Eliad et al. have shown that the molecular sieving effect appears when the size of ions approaches the pore size of carbon. For example, in the case of aqueous magnesium sulfate electrolyte, where the size of hydrated ions (Mg^{2+} and SO_4^{2-}) is larger than the average pore size of carbon (0.51 nm), less capacitive current is obtained.[13,14] In this respect, one could infer that maximum capacitance can be achieved with a large number of ions fitting to the pores and by this way taking full advantage of ion versus pore compatibility aspect.[15] Leaving aside the discussion related with a particular probe (e.g., nitrogen) for estimating surface and pore sizes, one would still argue over the importance of pore and ion size compatibility, which is further evidenced when ionic liquids are used as electrolytes for charge storage in nanoporous carbons.[16,17]

Received: November 20, 2020
Accepted: January 7, 2021
Published: January 19, 2021

https://dx.doi.org/10.1021/acsaem.0c02908
ACS Appl. Energy Mater. 2021, 4, 1763−1773

More importantly, it has been found that the majority of pores of carbon are underused due to their small size compared to the effective size of ions as well as their orientation while entering the pore.[18]

From the foregoing, it is clear that pore tuning in carbon materials is essential, and efforts in this direction have yielded little progress so far. Indeed, high-temperature and -pressure treatment of a zeolite template carbon resulted in reduced average micropore size; however, similar changes in density and pore texture were not observed for commercial carbons.[19] Templated carbons, on the other hand, give control of microporous structure and pore interconnectivity in carbon owing to the structural regularity possessed by the incorporated template materials.[20−22] However, high synthesis cost and the use of aggressive acids such as HF to remove the template materials hinder the viability of this method.

This work presents a new strategy to control the porosity of carbons by first obtaining a precursor with highly refined pores, setting the guideline for the porosity of final carbon product. In addition to other advantages, producing hydrogels from cross-linked polymers is environmentally friendly, nontoxic, and cheap. Cross-linked porous polymers offer a great opportunity to control porous structure, surface area, and adsorption properties.[23,24] As a result of the controlled porosity at different length scales, such materials possess interconnected pore structure that facilitates the diffusion of ions and molecules.[25] Previously, polymer-based precursors have been carbonized and activated to prepare carbons and some of them have been efficiently used for charge storage application.[26−30] However, no systematic porous texture was studied owing to the absence of predefined precursor's structural footprints. Here, we show the use of cross-linked polymer-based precursor to obtain carbons with a wide range of pore diameter fitting the size of the maximum number of ions and efficiently charging the EDL (Figure 1), and then preparing precursor composites with graphene to further improve the charge storage capability of these carbons.[31−33]

EXPERIMENTAL SECTION

Preparation of Nanoporous Carbons. An aqueous solution of poly(vinyl alcohol) (PVA) was prepared at a concentration of 10 wt %, and then poly(vinyl pyrrolidone) (PVP) was added to the solution while gradually increasing its mass ratio to PVA. Hydrochloric acid (37%) was added at a volume ratio of 1.5:100 to the aqueous mixture of PVA and PVP as the cross-linking agent.[34] The molecular weight of used PVA and PVP were 89 000−98 000 and 10 000, respectively.

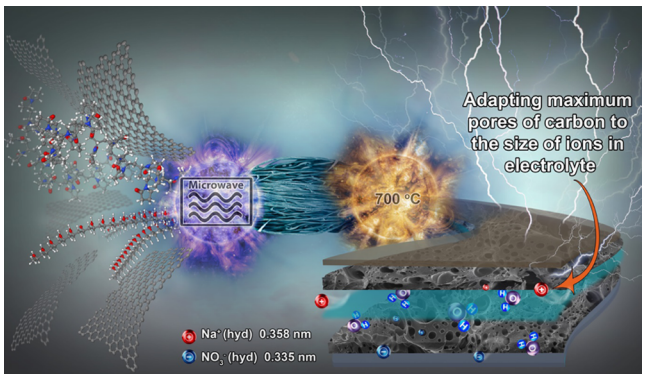

Figure 1. Cross-linking of polymers and formation of hydrogel via microwave irradiation. The porous hydrogel is then subjected to carbonization and activation at a high temperature to prepare nanoporous carbons with majority of pores adaptable for ionic transport and to gain maximum charge storage.

The mixtures were sonicated for 30 min and then stirred using magnetic stirring for another 30 min at room temperature to obtain a respective homogeneous dispersion. Each solution with fully dispersed components was then transferred to a microwave reactor (Anton Paar Synthos 3000 multimode reactor) at a 1400 W magnetron power, equipped with a wireless pressure and temperature sensor. The reactor was operated in the pressure mode using a power of 500 W; the sample temperature was ramped at 10 °C min^{-1} up to 190 °C and kept at this temperature for different reaction times. The schematic diagram for the preparation process of activated carbons is shown in Figure S1 (Supporting Information). For the second type of precursor sample, graphene prepared by chemical vapor deposition (CVD)[35] at lab scale was introduced to the initial mixture of PVP and PVA (4:6) and all composition was subjected to microwave irradiation. The cross-linked hydrogel material exhibited a consistent structure with or without graphene incorporated into it. The composites without graphene were first activated with KOH at 700, 800, and 900 °C to select a suitable activation temperature. Afterward, the PVP/PVA hydrogels with and without graphene were carbonized and activated at 700 °C (best activation temperature). The obtained carbon materials after the activation process were further cleaned with diluted hydrochloric acid and then dried at 120 °C for 12 h to remove water contents before further physicochemical investigations. To compare the surface area, 10 wt % PVP was also carbonized and activated at 700, 800, and 900 °C, and the obtained carbon materials were washed and cleaned in a similar manner to that mentioned previously. For the electrochemical investigations, the selected samples were post-treated at 700 °C for 1 h under nitrogen atmosphere to remove any remaining oxygenated functional groups from the surface of carbons.

Structural Characterization of Nanoporous Carbons. Nitrogen adsorption−desorption isotherms were measured at −196 °C using a Micromeritics ASAP 2020. Before analysis, samples (80 mg each) were degassed at 140 °C for 12 h under vacuum. The surface area was calculated by the Brunauer−Emmett−Teller (BET) method from the adsorption branch in the relative pressure (P/P_0) range of 0.01−0.2. Selected samples were also characterized using powder X-ray diffraction (XRD) employing an X'Pert-PRO diffractometer (PANalytical BV, the Netherlands) with theta/theta geometry, operating a cobalt tube at 35 kV and 50 mA. The XRD patterns of all specimens were recorded in the 2θ range of 10.0−80.0° with a counting time of 5.240 s per step. The scanning electron microscope (SEM) images were obtained on a Zeiss Ultra Plus 55 field emission scanning electron microscope (FE-SEM) operated at an accelerating voltage of 2.0 kV. Raman spectroscopic analysis of the graphene and composite materials was performed using a T64000 micro-Raman spectrometer from HORIBA Scientific, Jobin Yvon Technology, equipped with a triple monochromator system to eliminate contributions from the Rayleigh line. All of the samples were analyzed with a 514 nm argon excitation laser with a power of 12 mW at laser exit to avoid thermal effects. Thermogravimetric analysis (TGA) was carried out using a TA Instruments Q600 Simultaneous DSC/TG, which measures the weight change in a material as a function of temperature or time under a controlled atmosphere. TGA samples were heated from room temperature to 1000 °C at a rate of 10 °C min^{-1}.

Electrodes Preparation and Electrochemical Investigation of Supercapacitors. For the preparation of electrodes, a mixture of active carbon materials 90 wt %, poly(tetrafluoroethylene) (PTFE) binder 5 wt % (from Sigma-Aldrich), and conductivity additive 5 wt % (SUPER C65 from TIMCAL) was homogenized and dispersed in pure ethanol, and the slurry was then uniformly rolled to prepare the electrode sheet. The electrodes were pasted on to the current collector and dried at 100 °C in an oven for 12 h to ensure complete evaporation of ethanol and adsorbed water. The electrochemical test of the symmetric cell was carried out in a two-electrode cell configuration using Swagelok-type cells with a mass loading of ∼5.0 mg for each electrode with a thickness of 0.15 mm and a diameter of

https://dx.doi.org/10.1021/acsaem.0c02908
ACS Appl. Energy Mater. 2021, 4, 1763−1773

8.0 mm, using a glass microfiber filter paper as the separator soaked in a 5 mol L^{-1} $NaNO_3$ aqueous electrolyte solution. Electrochemical measurements such as cyclic voltammetry (CV), galvanostatic charge/discharge (galvanostatic cycling with potential limitation (GCPL)), and electrochemical impedance spectroscopy (EIS) at various voltages were carried out on an SP-300 potentiostat from Bio-Logic. The CV tests were carried out in the potential range of 0−1.6 V at different scan rates ranging from 2 to 200 mV s^{-1} and GCPL from 0.2 to 5 A g^{-1}, and electrochemical impedance spectroscopy (EIS) measurements were conducted in the frequency range of 1 mHz to 100 kHz at open-circuit voltages (OCVs) of 0.8, 1.0, 1.2, 1.4 and 1.6 V.

The galvanostatic charge−discharge tests based on the two-electrode cell was used for the evaluation of specific capacitance (C_{sp}: F g^{-1}), area capacitance (C_{area}: F cm^{-2}), area energy density (E_a: Wh cm^{-2}), and area power density of the cell (P_a: kW cm^{-2}) calculated using eqs 1 to 3. Generally, the full capacitance (CF) of a supercapacitor device is the manifestation of the electrical charge ΔQ stored at a given voltage change ΔV and can be used for the evaluation of supercapacitor performance[36,37]

$$C = \frac{I\Delta t}{\Delta V} \tag{1}$$

Nonetheless, the intrinsic specific capacitance of a single electrode in a symmetric cell is the preferred parameter, which estimates the charge storage capability of electrode materials and is expressed as

$$C_{sp} = \frac{4C}{m} \tag{2}$$

$$C_{sa} = \frac{C}{SA} \tag{3}$$

where C_{sp} (F g^{-1}) is the specific capacitance, C_{sa} is the capacitance per SA, I (A) is the charge/discharge current, ΔV (V) stands for the potential window within the discharge time Δt (s), m (g) corresponds to the amount of active material on the electrode, and SA is the surface area of the electrodes.

The corresponding specific energy, areal energy, specific power, and areal power for the symmetric cell are calculated according to eqs 4 and 7

$$E_{max} = \frac{1}{2}C(\Delta V)^2 = \frac{1000 \times C_{sp} \times \Delta V^2}{2 \times 4 \times 3600} = \frac{C_{sp} \times \Delta V^2}{28.8} \tag{4}$$

$$E_{areal} = \frac{1}{2}C(\Delta V)^2 = \frac{C_{sa} \times \Delta V^2}{2 \times 4 \times 3600 \times A} \tag{5}$$

$$P_{max} = \frac{3.6 \times E_{max}}{\Delta t} \tag{6}$$

$$P_{areal} = \frac{3.6 \times E_{areal}}{\Delta t} \tag{7}$$

RESULTS AND DISCUSSION

Synthesis and Characterization of Cross-Linked Polymer-Based Carbons. At the first step, a reduction reaction between PVA and PVP polymers was carried out to produce hydrogels via a simple microwave-assisted technique. Production of hydrogels by cross-linking of PVA and PVP is well known in the literature;[31−33] however, the use of microwave has been rarely reported. Microwave irradiation helps us to create radical sites at the −OH groups of PVA and/or at the main carbon chain of polymer, which participate in cross-linking via hydrogen bonding (Figure 2). For the second part, an aqueous suspension of PVA and PVP was prepared with graphene as an additive and the mixture was subjected to microwave treatment. The same reaction mechanism follows

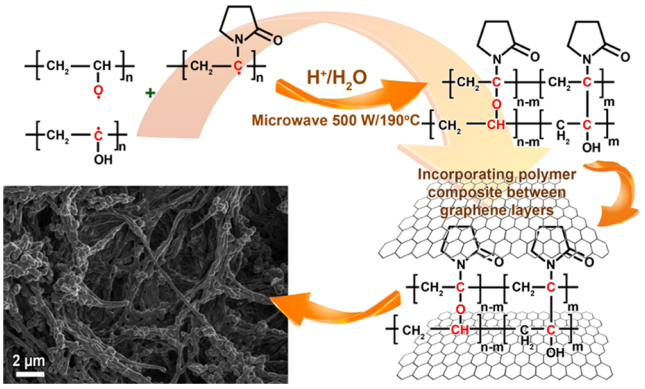

Figure 2. Reaction between PVP and PVA assisted by microwave irradiation to form polymer hydrogel with and without graphene addition. The two composite materials are then processed through chemical activation. The addition of graphene facilitates maintaining the porous structure and prevents structural collapse of interlayer spacing.

the generation of radical, and hydrogel incorporated with graphene was obtained, which was ready to be subjected to carbonization and activation. The activation was performed by KOH, where an alkali-to-composite material mass ratio of 1:3 was maintained. The activation was performed at three temperatures, i.e., 700, 800, and 900 °C, to select the most effective value with regard to carbon characteristics and performance parameters.

The internal three-dimensional networks observed for the hydrogel sample in Figure 3a show the high connectivity of

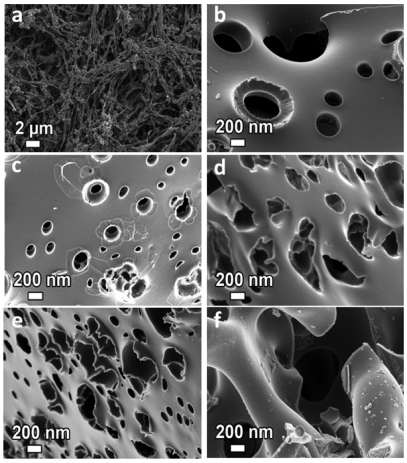

Figure 3. (a) SEM images of PVP/PVA hydrogel before activation and carbonization, then gradual increase of PVP-to-PVA, ratio, and after activation: (b) 1:9, (c) 2:8, (d) 3:7, (e) 4:6, and (f) 5:5.

fibers and the presence of preliminary pores in the polymer structure. The hydrogel material under the activation and carbonization conditions transformed into an excessive network of channels, evolving new pore structures. The creation of such channels is expected owing to the release of gases (CO, H_2O, and CO_2), which are formed initially during the carbonization stage and then chemical activation.[38,39] With an increase of the PVP ratio, the transport channels were clearly visible and the large pores appeared on the surface (Figure 3b−f). These big channels or network of pores lead to smaller pores within the carbon matrix, providing facile access

https://dx.doi.org/10.1021/acsaem.0c02908
ACS Appl. Energy Mater. 2021, 4, 1763−1773

to the bulk carbon material. Overall, the development of pore structure is progressive in nature owing to the increasing fraction of PVP to the PVA solution, which improves the pore morphology at the hydrogel precursor level (Figure S2 in the Supporting Information). Thanks to the initial pore structure of the hydrogel formed by the reaction of PVA and PVP, general wide-surfaced sheetlike structures are observed after activation with different PVP ratios from 1:9 to 4:6, as seen in the SEM images. A further increase in the PVP ratio to 5:5 (Figure 3f) results in a totally different structure of hydrogel, which has a more solid form and is unsuitable for preparing porous carbon.

The nitrogen gas adsorption isotherms for the carbons obtained by the activation of PVA (10 wt %) alone at a different temperature to find the best sample preparation condition are presented in Figure S3. The sample obtained at 700 °C has the highest BET surface area (Table 1) and

Table 1. BET Surface Area versus Carbonization Temperature of PVA (10 wt %) Sample

T_C[a]	700 °C	800 °C	900 °C
BET (m^2 g^{-1})	537	449	85

[a]Temperature at which PVA is carbonized and activated.

possesses a large number of small pores (0.204 cm^3 g^{-1} micropore volume for a total pore volume of 0.307 cm^3 g^{-1}). The shape of the adsorption/desorption isotherm also suggests the presence of mainly micropores, and reversibility is a direct indication of good pore connectivity and the presence of adjacent channels. Further enhancing the activation temperature to 800 and 900 °C causes the reduction of surface area and blockage of pores indicated by the sharp rise of isotherm in the high-pressure region. Activation by chemicals at a higher temperature may block access to micropores, which is also indicated by decreased surface area.[40,41] Hence, for preparing further carbon materials in this work, an activation temperature of 700 °C was selected. To obtain carbons with an appropriate and well-organized pore structure, hydrogel samples with varying percentages of PVP were subjected to carbonization and activation. This method was also helpful to obtain the optimum ratio of PVA to PVP, and its effect on the surface area of the resulting activated carbon was investigated. The first four carbon samples (from 1:9 to 4:6) with increasing fraction of PVP show the reversible Type I isotherm (Figures 4a–c and S4a), which is normally associated with microporous solids having relatively small external surfaces. Their limiting uptake of nitrogen is generally governed by the accessible micropore volume rather than by the surface area. Hence, a large surface area is represented by the high micropore volume and the presence of interconnected pores.

The sample with a PVA-to-PVP ratio of 5:5 shows a deviation of the adsorption and desorption curves from the previous trend (Figure 4d). However, such an isotherm could feature the Type H3 loop, which is generally associated with monolayer coverage and the start of multilayer sorption on nonporous materials. In this case, however, it indicates the Type I isotherm, characteristic for the presence of micropores in the carbon material together with the external surface remaining for further adsorption. Indeed, the inflection point appears in the sample with 60% PVP representing also the Type H3 loop (Figure 4e), which is observed for materials

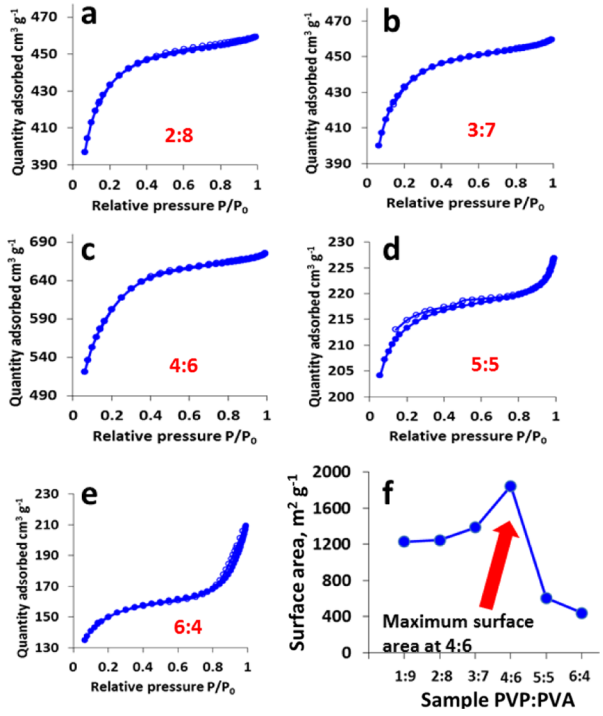

Figure 4. (a–e) Nitrogen gas adsorption/desorption isotherms of various samples with increasing mass ratio of PVP to PVA at a carbonization/activation temperature of 700 °C. (f) BET surface areas of different samples with increasing ratio of PVP and a maximum at the PVP-to-PVA ratio of 4:6 (reaching a surface area of 1846 m^2 g^{-1}). The filled and hollow circles in isotherms represent, respectively, the adsorption and desorption of nitrogen at −196 °C and relative pressure P/P_0 = 0.0 to 1.0.

with aggregates of platelike particles giving rise to slitlike pores.[42−44]

Combining now the observation from SEM data and N_2 gas adsorption/desorption isotherms, the following assumptions have been made. The broken platelet shape is present without a continuous external surface structure. The end of one of the sheets of the carbon sample with a PVP-to-PVA ratio of 4:6 shows a "cheddar-cheese"-like structure with a corresponding width of about 3 μm. This is indicative of the presence of a large number of small pores with respect to the other carbon samples investigated. Although the surface observation of the different carbon samples shows the presence of pores, there is an increasing degree of pore coverage with an increase in the proportion of PVP introduced to preliminary composition. This means that the carbon material obtained from a hydrogel with a PVP/PVA ratio of 4:6 exhibits the highest pore coverage. An exception is also found in the last samples with PVP/PVA ratios of 5:5 and 6:4, which did not exhibit definite pore structures. Keeping in view the N_2 sorption curve, one can infer that the slitlike pores are expected to be found for such structures.

For all of the prepared carbons, uneven sizes of pores for ratio 1:9–4:6 are clearly visible. Large nanometer-sized pores in the range of 400–600 nm are mostly exhibited by the 1:9 sample; these sizes decrease with the 2:8 sample, which showed mostly 200–300 nm diameter pore sizes. The carbons obtained after activation of 3:7 and 4:6 samples both possess large pore diameters looking like "pores-within-pores" structures. The carbon material from 4:6 samples still retains some of the singular 100 nm diameter big pores and an average

https://dx.doi.org/10.1021/acsaem.0c02908
ACS Appl. Energy Mater. 2021, 4, 1763−1773

pore diameter of 2.36 nm (Table S1 in the Supporting Information). The specific surface area values increase steadily for the carbon samples with PVP-to-PVA ratios of 1:9−4:6 with a sharp decline at ratio 5:5, as also seen from the BET values (Figure 4f and Table 2). The SEM images show the

Table 2. Increasing the Mass Ratio of PVP to PVA (for Preparing the Precursor Hydrogel Material) versus the BET Surface Area of Derived Carbons

sample	1:9	2:8	3:7	4:6	5:5	6:4
BET (m^2 g^{-1})	1230	1249	1347	1846	606	440

availability and morphology of the pores (Figure S5 in the Supporting Information), which follows a similar pattern to the values of obtained specific surface area. The carbon samples with a large number of pores and with more complicated structures give an insight into the rate at which gases evolve from the surface of the carbon sample during activation of the corresponding "parent hydrogel." This clearly shows the richness of the porosity and subsequent surface area of obtained carbon materials. Hence, by systematically varying the precursor composition, we can confirm that majority of bulk precursor material has been utilized for pore development.

Influence of Graphene as an Additive on the Textural Properties of Carbon. At the next stage, lab-scale-produced graphene was introduced to the polymer-based hydrogel precursor to enhance the conductivity and elaborate the pore structure. For this purpose, graphene was used as an additive to the initial mixture of PVP-to-PVA mass ratio of 4:6 before the microwave treatment. As shown in Figure 2, the interaction with graphene gives structural stability and improves the pore architecture, thereby retaining the integrity of electrode materials via enhanced pore connectivity and easy access to the transport channels within the carbon matrix. A gradual increase of graphene mass ratio to the total mixture of PVP/PVA did not alter the morphology of the hydrogel obtained after microwave treatment. Therefore, one can expect the evolution of a similar pore structure in the hydrogel before it goes through KOH activation. As seen in Table 3, a gradual increase of graphene from 0.0081 wt/wt % (0.010 wt/vol %) to 0.024 wt/wt % (0.030 wt/vol%) results in an enhanced surface area of the carbon material obtained after carbonization and activation at 700 °C. Figure 5 shows the simultaneous gas adsorption isotherm and thermogravimetry (TG) data of each sample obtained after activation of the three-component mixture of PVP/PVA (4:6) with graphene at varying mass proportion. The sample without the addition of graphene exhibits a surface area of 1846 m^2 g^{-1}. The use of graphene improves the surface area of the resulting composite material

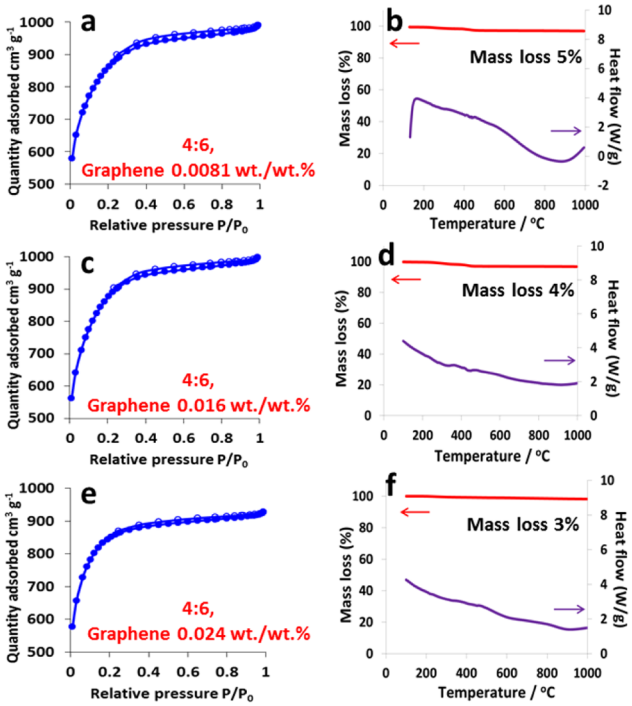

Figure 5. Nitrogen gas adsorption/desorption isotherms and thermogravimetric data for nanoporous carbon samples obtained from a PVP/PVA (4:6) composite with increasing proportion of graphene (a, b) 0.0081 wt/wt %, samples named in Table 3 as C46P-G10, (c, d) 0.016 wt/wt %, sample named as C46P-G20, and (e, f) 0.024 wt/wt %, sample named as C46P-G30—carbonized and activated at 700 °C, and various analyses performed on the materials: (a, c, e) gas adsorption characterization and (b, d, f) thermogravimetric analysis.

up to ca. 3100 m^2 g^{-1}. The additional benefit of using graphene with polymer structure is to incorporate it within a layer structure (evident from the low mass loss of ∼4% in TGA curves), and the presence of such an architecture preserves the integrity of carbon materials and keeps the channels open for ionic transport.

One can see that the combination of PVP/PVA with graphene not only improves the surface area and alters the pore structure but also enhances pore connectivity and gives control over the pore alignment (Figure S6). This aspect is crucial for designing efficient charge storage systems where the compatibility of ion sizes with the size of pores is important.[45−47] As expected, the addition of graphene to the hydrogels increases their surface area and conductivity. With an increased amount of 0.016 wt/wt % of graphene, a surface area of up to 3107 m^2 g^{-1} is achieved (Table 3). However, a further increase of graphene content does not influence to a

Table 3. Table 2 Porous Textural Data of Activated Carbons Obtained from Different Proportions of wt % of Graphene in a Mixture of PVP and PVA (4:6) at Activation Temperature T_C = 700 °C[d]

sample	wt/wt % of graphene	wt/vol % of graphene	BET [m^2 g^{-1}]	[a]V_{micro} [cm^3 g^{-1}]	[b]V_{total} [cm^3 g^{-1}]	[c]pore diameter [nm]
C46P			1846	0.50	1.04	2.36
C46P-G10	0.008	0.01	2848	0.51	0.84	2.40
C46P-G20	0.016	0.02	3107	0.56	0.88	2.35
C46P-G30	0.024	0.03	2998	0.52	0.70	2.21

[a]*t*-Plot micropore volume. [b]BJH desorption cumulative volume of pores of diameter between 1.7 and 300 nm. [c]BJH desorption average pore diameter (4 V/A). [d]For comparison, porous data of sample without graphene additive are given.

https://dx.doi.org/10.1021/acsaem.0c02908
ACS Appl. Energy Mater. 2021, 4, 1763−1773

greater extent the specific surface area and the pore architecture, which is indicated by the sample containing 0.024 wt/wt % graphene. The presence of micropore volume in the range of 0.5 cm^3 g^{-1} is similar to most commercial carbons; however, the presence of graphene sheets and their layer-by-layer connectivity with preserved stacking properties gives access to even small micropores, which enhance the surface area.[48,49] Moreover, a well-distributed pore size range makes these carbons suitable for preparing sustainable electrodes for supercapacitors, which have been investigated and discussed in the next section.

Performance of Nanoporous Carbons in Symmetric Supercapacitors. The electrochemical performances of symmetric supercapacitors using two types of carbon samples (i) a PVP-to-PVA mass ratio of 4:6 (referred to in this section as PVP + PVA) and (ii) a PVP-to-PVA mass ratio of 4:6 with 0.016 wt/wt % of graphene (referred to in this section as PVP + PVA + graphene) were compared, and the results are summarized in Figure 6. Keeping in view the wide pore size distribution and pore diameter in the range of 2.36 nm, the alkali-metal ions and most of the inorganic cations would easily fit, resulting in fast charging of EDL. We selected $NaNO_3$-based electrolyte due to its easy availability, low cost, abundance, and, above all, the compatibility of ion size with

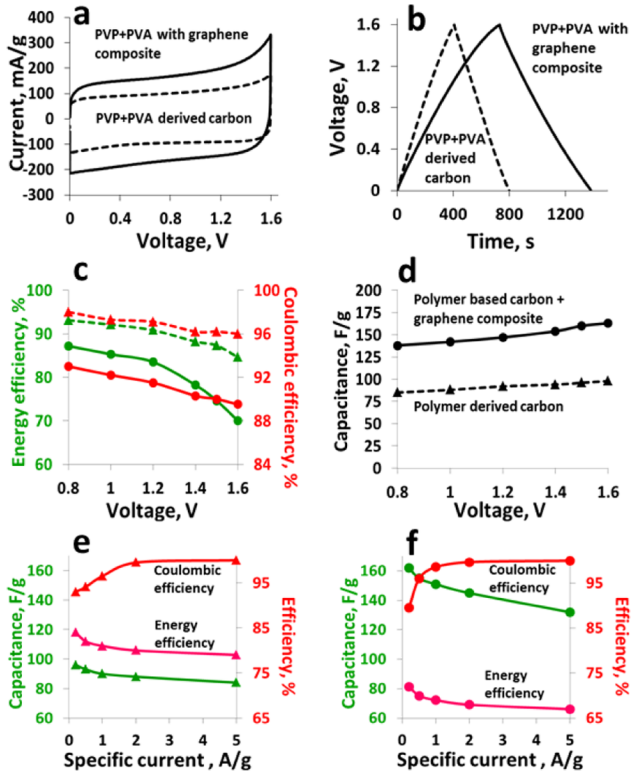

Figure 6. Electrochemical performance of symmetric capacitor using PVP + PVA and PVP + PVA + graphene electrodes in 5 mol L^{-1} $NaNO_3$. (a) Cyclic voltammetry at 0.2 mV s^{-1}; (b) galvanostatic charge/discharge at 0.2 A g^{-1}; (c, d) evolution of coulombic efficiency (η_c), energy efficiency (η_e), and capacitance versus voltage up to 1.6 V at 0.2 A g^{-1}; and capacitance, coulombic efficiency, and energy efficiency evolution at 1.6 V with increasing specific current up to 5 A g^{-1} for (e) PVP + PVA- and (f) PVP + PVA + graphene-based supercapacitor. The dashed line (with ▲) represents the PVP + PVA, and the solid line (with ●) represents the PVP + PVA + graphene-based supercapacitors.

a pore structure of designed carbons. The symmetric charge/discharge curves for a capacitor with PVP + PVA-based carbon at 0.2 A g^{-1} (Figures S9–S11 in the Supporting Information) and the nearly rectangular shape of CVs at a high scan rate of up to 200 mV s^{-1} from 0.8 to 1.6 V suggest the main charge storage phenomenon occurring at the electric double layer (EDL). Similarly, the second capacitor using PVP + PVA + graphene-based electrode also shows symmetric charge/discharge curves and excellent charge propagation up to 1.6 V and 200 mV s^{-1}. Nevertheless, due to the presence of water-based electrolyte, some contributions indicated by the current increase in CVs at the high-voltage region near 1.5 or 1.6 V are important, which correspond to the reversible adsorption/desorption (or reversible storage) of hydrogen in pores of the negative electrode material produced under the electrochemical reduction of water. Simultaneously, production of OH^- ions provokes increased local pH at the negative electrode, which provides a high overpotential for dihydrogen evolution, enabling the carbon/carbon supercapacitor to operate beyond the stability window of water (E° = 1.23 V).[50]

However, these faradic processes represent only a fractional contribution to the total capacitance of the supercapacitor. Certainly, the main capacitance in both the systems originates from charge storage at the EDL. The comparison of CVs (Figure 6a) and galvanostatic charge/discharge (Figure 6b) between the two capacitors confirms the high capacitance for the system with an electrode containing graphene as an additive. One can also see that, despite the low capacitance for the cell using the PVP + PVA-based electrode, the shape of the CV and GCPL curves is more symmetric, suggesting EDL charging as the main charge storage phenomenon. In particular, the rectangular shape of CV and symmetric GCPL for the PVP + PVA-based sample up to 200 mV s^{-1} and 5 A g^{-1} (Figure S9) indicates the total charge storage at the EDL, which is a highly reversible and physical phenomenon and involves very little contribution from the electrochemical reduction/oxidation of water at the negative or positive carbon electrodes. Thanks to the polymeric structure preserving the electrode porous structure, a very fast charge and discharge can be achieved and thereby an enhanced rate performance of the supercapacitor device. A low ohmic loss in charge/discharge curves is evident of good pore connectivity and transport channels within the electrode matrix for ionic movement. As the triangular shape of charge/discharge curves is conserved even at high specific currents, one can infer the high rate capability and cycle life of supercapacitor using this electrode material.

Figure 6c–f shows the comparison of coulombic efficiency (ratio of discharge time to charging time), energy efficiency (ratio of area under discharge curve to the area under charging curve), capacitance, and, rate performance. Relatively high values of energy efficiency (89%) and coulombic efficiency (96%) at 1.6 V (at 0.2 A g^{-1} in Figure 6c) for the cell with PVP + PVA-based electrodes suggest easy ionic transport within the channels and without substantial loss of charges in the faradic processes. This is also evidence of fast charging/discharging of EDL in the case of the PVP + PVA-based capacitor. On the other hand, for the supercapacitors with PVP + PVA + graphene-based electrodes, the energy efficiency value is 73% and the coulombic efficiency value is 89% at 1.6 V (at 0.2 A g^{-1}). The relatively low efficiency values suggest the presence of deep channels between the graphene layers with slight

https://dx.doi.org/10.1021/acsaem.0c02908
ACS Appl. Energy Mater. 2021, 4, 1763–1773

coverage due to the functional groups, which may hinder the swift movement of ions upon charge and discharge.

The capacitance comparison in Figure 6d and the evolution of capacitance versus increasing specific current (Figure 6e,f) suggest a high rate performance of supercapacitor constructed using the PVP + PVA electrode material. Although the capacitance value for the supercapacitor with the PVP + PVA + graphene electrode is high (163 F g^{-1} at 0.2 A g^{-1}), the capacitance decreases by 18% when increasing current from 0.2 to 5 A g^{-1}. This is also indicated by the low energy efficiency of supercapacitor using this material, ∼66% at 5 A g^{-1} compared to ∼79% for the PVP + PVA-based cell. Although the hydrogen adsorption and desorption are reversible at low cell voltages, indeed the irreversibility contributes to the loss of efficiency due to more charges consumed at high voltages. Besides, the low energy efficiency for the cell using electrode material with graphene additive suggests a different pore architecture and the presence of functional groups.

The Nyquist plot, which is the frequency response of the device with imaginary and real impedances as a function of frequency, is shown in Figure 7. The high-frequency

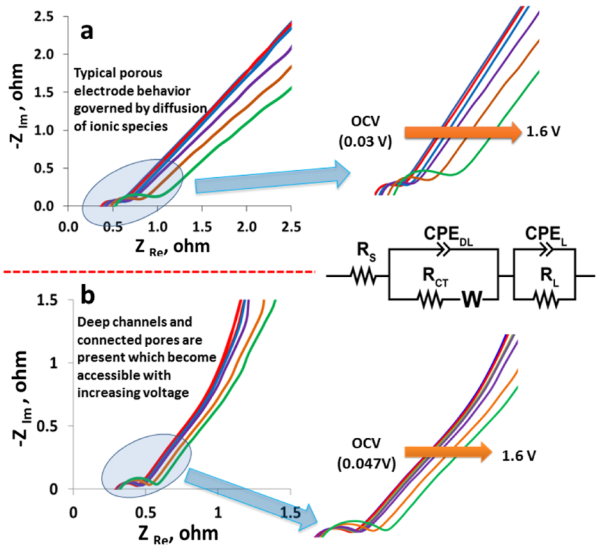

Figure 7. (a) Nyquist plots obtained at different voltages from open-circuit voltage up to 1.6 V for symmetric capacitors using (a) PVP + PVA-based electrodes and (b) PVA + PVP + graphene electrodes in 5 mol L^{-1} $NaNO_3$. The insets in (a) and (b) show the enlarged high-frequency region of Nyquist plots and an equivalent circuit model representing both systems. The color representation for voltages is as follows: Red (OCV), light blue (0.8 V), yellow (1.0 V), blue (1.2 V), purple (1.4 V), orange (1.5 V), and green (1.6 V).

intersection with the positive *Z*-axis shows a semicircle at this frequency domain, a 45° line region, and a vertical line in the low-frequency region, typically signifying the charge storage mechanisms of the capacitive materials (Figures S12 and S13). The presence of functional groups on the surface of the carbon materials may contribute to the charge transfer process that arises from an electron transfer from one phase (e.g., electrode) to another (e.g., liquid). In addition, interfacial impedances between the current collector/active material may also contribute to the appearance of the semicircle.[51−53] This was confirmed by recording the impedance data at multiple potentials from the open-circuit potential to 1.6 V. The change in the charge transfer resistance (diameter of the semicircle) with increasing potential affirms the assertion that the main contribution is from a charge transfer process. The R_{ct} values range from 0.33 to 0.61 Ω for Figure 7a (PVP + PVA) and from 0.14 to 0.23 Ω for Figure 7b (PVP + PVA + graphene) as the voltage increases. Furthermore, the smaller values of R_{ct} obtained at high frequencies for the cell with PVP + PVA + graphene-based electrodes as the voltage increases is attributed to the increase in conductivity of the carbon material due to the presence of graphene and may increase electron mobility as the voltage increases, leading to a decrease in the diameter of the semicircle. The ESR values in Table 4 extracted from the Nyquist plot at 1 kHz show an increasing trend for both the capacitors from OCV to 1.6 V. Nevertheless, these values are smaller in PVP + PVA + graphene electrode-based capacitor than in PVP + PVA-based capacitor, owing to high interlayer connectivity in the latter. Additionally, the ESR values measured from the galvanostatic charge/discharge curves at 1 A g^{-1} (up to 1.6 V) also follow a similar pattern, with 0.381 Ω for PVP + PVA-based capacitor and 0.261 Ω for the capacitor with PVP + PVA + graphene electrodes.

Furthermore, the shift of the knee frequency region suggests the influence of increasing voltage on the ionic movement. The impeded movement of ions within the deeper pores is indicated by extended medium-frequency region. The equivalent circuit diagram obtained from the fitting of impedance data is presented for both systems in Figure 7. The EIS plots are fitted according to the Randles circuit model, which is ideal and close to practical application. The equivalent circuit element R_S represents the resistance of the electrolyte; R_{CT} is the resistance of the electrode−electrolyte interface; R_L is the leakage resistance, CPE_{DL} is the constant phase element (CPE) of double layer symbolizing the double-layer capacitance, which occurs at interfaces between the porous carbon and solution due to separation of ionic and/or electronic charges; and W is the Warburg element, which represents the diffusion of ions into the porous electrode in the medium-frequency region and is a consequence of the frequency requirement of the diffusion process. A probable attribute to the insensitivity to changing voltage is a short diffusion path length of the ions in the electrolyte, as evidenced by a short Warburg region on the Nyquist plots. R_L is the leakage resistance, which is placed in parallel with CPE_L, and it is usually very high and can be ignored in the circuit. CPE_L

Table 4. ESR and Time Constant (τ) Values for Symmetric Supercapacitors Using Either PVP + PVA or PVP + PVA + Graphene-Based Carbon Electrodes in 5 mol L^{-1} $NaNO_3$

		OCV	0.8 V	1.0 V	1.2 V	1.4 V	1.5 V	1.6 V
PVP + PVA	ESR (Ω)	0.543	0.580	0.620	0.631	0.664	0.798	0.982
	τ (s)	1.41	1.41	1.41	1.41	1.89	1.89	1.89
PVP + PVA + graphene	ESR (Ω)	0.438	0.438	0.451	0.460	0.472	0.524	0.575
	τ (s)	2.27	1.89	1.89	1.89	1.89	1.89	1.89

https://dx.doi.org/10.1021/acsaem.0c02908
ACS Appl. Energy Mater. 2021, 4, 1763−1773

represents the additional contribution to capacitance, which may arise from voltage-dependent faradic charge transfer processes.[54] The time constant calculated from the real capacitance versus frequency data[55] (Figures S14 and S15) for the two systems is presented in Table 4. Both the supercapacitors can be fully charged up to 1.6 V in a similar time of 1.89 s, which confirms the positive effect of graphene additive on the carbon nanostructure (despite high surface area) for improved rate performance.

Galvanostatic charge/discharge cycling tests of supercapacitor containing PVP + PVA- and PVP + PVA + graphene-based electrodes in a 5 mol L^{-1} $NaNO_3$ electrolyte at 1.6 V and a constant specific current of 1 A g^{-1} were performed (Figure 8). At the end of 10 000 galvanostatic charge/discharge cycles, capacitance remains constant (no capacitance decay) for the capacitor with PVP + PVA electrodes, while it decays by 4% for the cell with PVP + PVA + graphene-based electrodes. However, the energy efficiency estimated after every 1000 galvanostatic charge/discharge cycle improves by 2 and 4% after a total of 10 000 cycles for PVP + PVA- and PVP + PVA + graphene-based systems, respectively. The improved energy efficiency could be due to the enhanced wetting of electrode and gradual ion transport into the deep pores of the electrodes. In particular, for the PVP + PVA-based capacitor, the constant capacitance and efficiency values suggest the stability of the supercapacitor device to operate at a high voltage and with negligible degradation to the electrodes. A comparison of galvanostatic charge−discharge curves at 1 A g^{-1} before and after cycling shows superimposition of curves corroborating the high stability of the system, where both cells maintain nearly the initial "fresh cell-like" characteristics. The energy and power performance estimated from galvanostatic charge/discharge up to high specific currents is shown in the Ragone plot (Figure 8d), where PVA + PVP- and PVA + PVP + graphene-based capacitors demonstrate high energies of 8 and 12 Wh kg^{-1}, respectively, at a specific power of 2 kW kg^{-1} (Table S2). Furthermore, the surface area of carbons obtained from activation of polymeric sources and the performance of thereafter-built supercapacitors in aqueous electrolytes are compared in Table 5. The high surface area and capacitance values obtained for carbons prepared in this work closely match and, in some cases, exceed the performance of state-of-the-art systems.

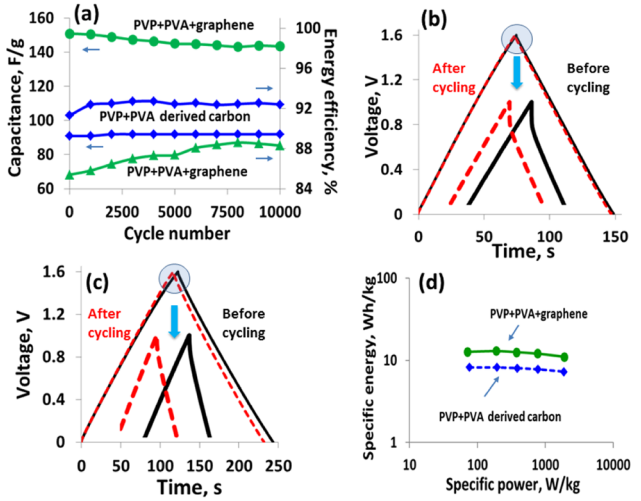

Figure 8. (a) Electrochemical stability test of supercapacitors for 10 000 galvanostatic charge/discharge cycles at 1.0 A/g. Comparison of galvanostatic charge/discharge curves before and after cycling at 1 A/g for (b) PVP + PVA carbon-based supercapacitor and (c) PVP + PVA + graphene composite-based supercapacitor. (d) Ragone plot showing the comparison of energy and power performances for symmetric supercapacitors with two carbon materials. The data for Ragone plot are extracted from the galvanostatic charge/discharge curves at 0.2, 0.5, 1, 2, and 5 A g^{-1} up to 1.6 V in Figure S9.

CONCLUSIONS

Nanoporous carbons derived from the composite of PVP and PVA represent an eco-friendly and low-cost route to prepare electrode materials. The systematic variation of polymeric components gives control over the evolution of porous texture, which can be adapted for charge storage applications. Interestingly, the chemical reaction via microwave irradiation resulting in hydrogel gives control over porosity at the precursor level. By introducing graphene additives to the preliminary composite before activation, certain physicochemical and electrochemical properties of the carbon material can

Table 5. Comparison of Surface Area, Capacitance, and Energy Density of Supercapacitors Using Polymer-Derived Carbons in Aqueous Electrolytes[a]

materials	specific surface area (m^2 g^{-1})	specific capacitance (F g^{-1})	energy density (Wh kg^{-1})	ref
low-density polyethylene (LDPE)-derived activated carbons (PE-AC)	1600	112		56
Phenolic resin	1759	115		57
graphene foam/polyvinyl alcohol/formaldehyde (GF/PVA/FP and GF/PVA/F)	705	158		58
	610	177		
nitrogen-doped hollow carbon spheres		173		59
lignin-based hierarchical porous carbon	1140	148 at 0.2 A g^{-1}		60
sodium lignosulfonate	1867	370 at 0.5 A g^{-1}	18.5	61
block copolymer	2104	257 at 0.5 A g^{-1}		62
block copolymers	953	150 at 0.625 A g^{-1}		63
polyacrylonitrile	451	156 at 0.2 A g^{-1}		64
eucalyptus-bark	1276	155	32.8	65
lecithin	1803	285 at 0.5 A g^{-1}	24.7	66
PVP + PVA + graphene	3107	163 at 0.2 A g^{-1}	12	this work

[a]Capacitance values in this work have been calculated according to the method proposed by A. Laheäär et al.[67]

https://dx.doi.org/10.1021/acsaem.0c02908
ACS Appl. Energy Mater. 2021, 4, 1763−1773

be altered. Also, the addition of graphene improves the surface area and pore connectivity, which in turn provides facile transport channels for ionic movement. The charge/discharge curves of symmetric supercapacitors confirm that by adapting the majority of pores to the size of ions, the performance of the supercapacitor device can be improved. The outstanding energy and power parameters of supercapacitors show great potential for the application of these materials in high-power-related applications. Hence, designing materials with pores adaptable to ion size are crucial for next-generation high-power devices. Future work is aimed at designing new carbons based on these reaction pathways and activation processes by the use of different polymeric chain lengths to create new pore architectures that could accommodate bigger ions, e.g., ionic liquid-based electrolytes.

■ ASSOCIATED CONTENT

Supporting Information

The Supporting Information is available free of charge at https://pubs.acs.org/doi/10.1021/acsaem.0c02908.

Steps during preparation of carbons; gas adsorption data of carbons; SEM images of carbons; porous textural data of carbons; Raman and XRD spectra of selected carbon samples; and electrochemical performance comparison of supercapacitors (PDF)

■ AUTHOR INFORMATION

Corresponding Authors

Farshad Barzegar − *Electrical, Electronic and Computer Engineering Department, University of Pretoria, Pretoria 0002, South Africa*; Email: farshadbarzegar@gmail.com

Qamar Abbas − *Institute for Chemistry and Technology of Materials, Graz University of Technology, 8010 Graz, Austria*; orcid.org/0000-0002-1169-1906; Email: qamar.abbas@tugraz.at

Authors

Vladimir Pavlenko − *Al-Farabi Kazakh National University, 050040 Almaty, Kazakhstan*

Muhammad Zahid − *Department of Chemistry, University of Agriculture, 38000 Faisalabad, Pakistan*

Abdulhakeem Bello − *Department of Theoretical and Applied Physics, African University of Science and Technology, Abuja, Nigeria; Department of Physics, University of Pretoria, Pretoria 0002, South Africa*

Xiaohua Xia − *Electrical, Electronic and Computer Engineering Department, University of Pretoria, Pretoria 0002, South Africa*

Ncholu Manyala − *Department of Physics, University of Pretoria, Pretoria 0002, South Africa*; orcid.org/0000-0003-2990-4284

Kenneth I. Ozoemena − *School of Chemistry, Molecular Science Institute, University of the Witwatersrand, Johannesburg 2050, South Africa*; orcid.org/0000-0001-7107-7003

Complete contact information is available at: https://pubs.acs.org/10.1021/acsaem.0c02908

Author Contributions

Q.A. and F.B. conceptualized the work. F.B. prepared and characterized carbon materials. F.B., V.P., and M.Z. performed physicochemical data analysis. F.B. conducted electrochemical investigations and data analysis supported by Q.A. F.B., V.P., and M.Z. wrote the first draft, and A.B., X.X., N.M., K.O., and Q.A. reviewed the final manuscript.

Notes

The authors declare no competing financial interest.

■ ACKNOWLEDGMENTS

This work was supported by the National Research Foundation of South Africa (grant no. 61056). The findings and recommendations expressed in this work are those of the authors, and the NRF does not accept any liability in this regard. Q.A acknowledges the Austrian Science Fund (FWF) for granting Lise Meitner project M2576-N37 and support from Bernhard Gollas, Ilie Hanzu, and Martin Wilkening.

■ REFERENCES

(1) Pomerantseva, E.; Bonaccorso, F.; Feng, X.; Cui, Y.; Gogotsi, Y. Energy storage: The future enabled by nanomaterials. *Science* **2019**, *366*, No. eaan8285.

(2) Borenstein, A.; Hanna, O.; Attias, R.; Luski, S.; Brousse, T.; Aurbach, D. Carbon-based composite materials for supercapacitor electrodes: a review. *J. Mater. Chem. A* **2017**, *5*, 12653−12672.

(3) González, A.; Goikolea, E.; Barrena, J.; Mysyk, R. Review on supercapacitors: Technologies and materials. *Renewable Sustainable Energy Rev.* **2016**, *58*, 1189−1206.

(4) Gao, Y. Graphene and Polymer Composites for Supercapacitor Applications: a Review. *Nanoscale Res. Lett.* **2017**, *12*, No. 387.

(5) Borchardt, L.; Oschatz, M.; Kaskal, S. Tailoring porosity in carbon materials for supercapacitor applications. *Mater. Horiz.* **2014**, *1*, 157−168.

(6) Pipitone, E.; Vitale, G. A regenerative braking system for internal combustion engine vehicles using supercapacitors as energy storage elements - Part 1: System analysis and modeling. *J. Power Sources* **2020**, *448*, No. 227368.

(7) Zou, Z.; Cao, J.; Cao, B.; Chen, W. Evaluation strategy of regenerative braking energy for supercapacitor vehicle. *ISA Trans.* **2015**, *55*, 234−240.

(8) Baptista, J. M.; Sagu, J.; Wijayantha, K. G.; Lobato, K. State-of-the-art materials for high power and high energy supercapacitors: Performance metrics and obstacles for the transition from lab to industrial scale − A critical approach. *Chem. Eng. J.* **2019**, *374*, 1153−1179.

(9) Gratuito, M.; Panyathanmaporn, T.; Chumnanklang, R.; Sirinuntawittaya, N.; Dutta, A. Production of activated carbon from coconut shell: Optimization using response surface methodology. *Bioresour. Technol.* **2008**, *99*, 4887−4895.

(10) Foo, K.; Hameed, B. Preparation and characterization of activated carbon from pistachio nut shells via microwave-induced chemical activation. *Biomass Bioenergy* **2011**, *35*, 3257−3261.

(11) Kleszyk, P.; Ratajczak, P.; Skowron, P.; Jagiello, J.; Abbas, Q.; Frackowiak, E.; Béguin, F. Carbons with narrow pore size distribution prepared by simultaneous carbonization and self-activation of tobacco stems and their application to supercapacitors. *Carbon* **2015**, *81*, 148−157.

(12) Salitra, G.; Soffer, A.; Eliad, L.; Cohen, Y.; Aurbach, D. Carbon Electrodes for Double-Layer Capacitors I. Relations Between Ion and Pore Dimensions. *J. Electrochem. Soc.* **2000**, *147*, 2486−2493.

(13) Eliad, L.; Pollak, E.; Levy, N.; Salitra, G.; Soffer, A.; Aurbach, D. Assessing optimal pore-to-ion size relations in the design of porous poly(vinylidene chloride) carbons for EDL capacitors. *Appl. Phys. A* **2006**, *82*, 607−613.

(14) Eliad, L.; Salitra, G.; Soffer, A.; Aurbach, D. Ion Sieving Effects in the Electrical Double Layer of Porous Carbon Electrodes: Estimating Effective Ion Size in Electrolytic Solutions. *J. Phys. Chem. B* **2001**, *105*, 6880−6887.

(15) Li, Z.; Gadipelli, S.; Li, H.; Howard, C.; Brett, D.; Shearing, P.; Guo, Z.; Parkin, I.; Li, F. Tuning the interlayer spacing of graphene

laminate films for efficient pore utilization towards compact capacitive energy storage. *Nat. Energy* **2020**, *5*, 160−168.
(16) Ania, C. O.; Pernak, J.; Stefaniak, F.; Raymundo-Piñero, E.; Béguin, F. Solvent-free ionic liquids as in situ probes for assessing the effect of ion size on the performance of electrical double layer capacitors. *Carbon* **2006**, *44*, 3126−3130.
(17) Ortega, P. F. R.; A dos Santos, G., Jr.; Trigueiro, P.; Silva, G.; Quintanal, N.; Blanco, C.; Lavall, R.; Santamaria, R. Insights on the Behavior of Imidazolium Ionic Liquids as Electrolytes in Carbon-Based Supercapacitors: An Applied Electrochemical Approach. *J. Phys. Chem. C* **2020**, *124*, 15818−15830.
(18) Largeot, C.; Portet, C.; Chmiola, J.; Taberna, P. L.; Gogotsi, Y.; Simon, P. Relation between the Ion Size and Pore Size for an Electric Double-Layer Capacitor. *J. Am. Chem. Soc.* **2008**, *130*, 2730−2731.
(19) Matsuoka, K.; Yamagishi, Y.; Yamazaki, T.; Setoyama, N.; Tomita, A.; Kyotani, T. Extremely high microporosity and sharp pore size distribution of a large surface area carbon prepared in the nanochannels of zeolite Y. *Carbon* **2005**, *43*, 876−879.
(20) Hulicova, D.; Yamashita, J.; Soneda, Y.; Hatori, H.; Kodama, M. Supercapacitors Prepared from Melamine-Based Carbon. *Chem. Mater.* **2005**, *17*, 1241−1247.
(21) Hulicova, D.; Kodama, M.; Hatori, H. Electrochemical Performance of Nitrogen-Enriched Carbons in Aqueous and Non-Aqueous Supercapacitors. *Chem. Mater.* **2006**, *18*, 2318−2326.
(22) Inagaki, M.; Toyoda, M.; Soneda, Y.; Tsujimura, S.; Morishita, T. Templated mesoporous carbons: Synthesis and applications. *Carbon* **2016**, *107*, 448−473.
(23) Ding, L.; Gao, H.; Xie, F.; Li, W.; Bai, H.; Li, L. Porosity-Enhanced Polymers from Hyper-Cross-Linked Polymer Precursors. *Macromolecules* **2017**, *50*, 956−962.
(24) Zhu, J.-H.; Chen, Q.; Sui, Z-Y.; Pan, L.; Yu, J.; Han, B-H. Preparation and adsorption performance of cross-linked porous polycarbazoles. *J. Mater. Chem. A* **2014**, *2*, 16181−16189.
(25) Seo, M.; Kim, S.; Oh, J.; Kim, S-J.; Hillmyer, M. Hierarchically Porous Polymers from Hyper-cross-linked Block Polymer Precursors. *J. Am. Chem. Soc.* **2015**, *137*, 600−603.
(26) Yenisoy-Karakaş, S.; Aygun, A.; Gunes, M.; Tahtasakal, E. Physical and chemical characteristics of polymer-based spherical activated carbon and its ability to adsorb organics. *Carbon* **2004**, *42*, 477−484.
(27) Park, H. G.; Won Kim, T.; Yun Chae, M.; Yoo, I-K. Activated carbon-containing alginate adsorbent for the simultaneous removal of heavy metals and toxic organics. *Process Biochem.* **2007**, *42*, 1371−1377.
(28) Makromaski, G. Porous structure and thermal properties of carbon adsorbents from pitch−polymer compositions. *J. Therm. Anal. Calorim.* **2018**, *133*, 1345−1352.
(29) Raymundo-Piñero, E.; Leroux, F.; Béguin, F. A High-Performance Carbon for Supercapacitors Obtained by Carbonization of a Seaweed Biopolymer. *Adv. Mater.* **2006**, *18*, 1877−1882.
(30) Zhang, L.; Gu, H.; Sun, H.; Cao, F.; Chen, Y.; Chen, G. Molecular level one-step activation of agar to activated carbon for high performance supercapacitors. *Carbon* **2018**, *132*, 573−579.
(31) Kamoun, E. A.; Chen, X.; Mohy Eldin, M. S.; Kenawy, E.-R.S. Crosslinked poly(vinyl alcohol) hydrogels for wound dressing applications: A review of remarkably blended polymers. *Arabian J. Chem.* **2015**, *8*, 1−14.
(32) Swain, A. K.; Bahadur, D. Enhanced Stability of Reduced Graphene Oxide Colloid Using Cross-Linking Polymers. *J. Phys. Chem. C.* **2014**, *118*, 9450−9457.
(33) Zhang, L.; Zhang, F.; Yang, X.; Long, G.; Wu, Y.; Zhang, T.; Leng, K.; Huang, Y.; Ma, Y.; Yu, A.; Chen, Y. Porous 3D graphene-based bulk materials with exceptional high surface area and excellent conductivity for supercapacitors. *Sci. Rep.* **2013**, *3*, No. 1408.
(34) Bello, A.; Fashedemi, O. O.; Lekitima, J. N.; Fabiane, M.; Dodoo-Arhin, D.; Ozoemena, K. I.; Gogotsi, Y.; Charlie Johnson, A. T.; Manyala, N. High-performance symmetric electrochemical capacitor based on graphene foam and nanostructured manganese oxide. *AIP Adv.* **2013**, *3*, No. 082118.
(35) Guellati, O.; Janowska, I.; Bégin, D.; Guerioune, M.; Mekhalif, Z.; Delhalle, J.; Moldovan, S.; Ersen, O.; Pham-Huu, C. Influence of ethanol in the presence of H_2 on the catalytic growth of vertically aligned carbon nanotubes. *Appl. Catal., A* **2012**, *423−424*, 7−14.
(36) Balducci, A.; Belanger, D.; Brousse, T.; Long, J. W.; Sugimoto, W. Perspective—A Guideline for Reporting Performance Metrics with Electrochemical Capacitors: From Electrode Materials to Full Devices. *J. Electrochem. Soc.* **2017**, *164*, A1487−A1488.
(37) Zhou, J.; Lian, J.; Hou, L.; Zhang, J.; Gou, H.; Xia, M.; Zhao, Y.; Strobel, T.; Tao, L.; Gao, G. Ultrahigh volumetric capacitance and cyclic stability of fluorine and nitrogen co-doped carbon microspheres. *Nat. Commun.* **2015**, *6*, No. 8503.
(38) Derbyshire, F.; Jagtoyen, M.; Thwaites, M. Activated Carbons-Production and Applications. In *Porosity in Carbon*; Patrick, J. W., Ed.; Edward Arnold: London, U.K., 1995; p 227.
(39) Marsh, H.; Rodriguez-Reinoso, F. *Activated Carbon*; Elsevier Science & Technology Books, 2006; p 536.
(40) Shin, H.; Ryoo, R.; Kruk, M.; Jaroniec, M. Modification of SBA-15 pore connectivity by high-temperature. *Chemical Commun.* **2001**, 349−350.
(41) Lowe, J. B.; Baker, R. Deformation of Ordered Mesoporous Silica Structures on Exposure to High Temperatures. *J. Nanomater.* **2014**, *2014*, No. 754076.
(42) Wei, L.; Sevilla, M.; Fuertes, A. B.; Mokaya, R.; Yushin, G. Polypyrrole-Derived Activated Carbons for High-Performance Electrical Double-Layer Capacitors with Ionic Liquid Electrolyte. *Adv. Funct. Mater.* **2012**, *22*, 827−834.
(43) Sing, K. S. W.; Williams, R. T. Physisorption Hysteresis Loops and the Characterization of Nanoporous Materials. *Adsorpt. Sci. Technol.* **2004**, *22*, 773−782.
(44) Weidemann, S.; Kockert, M.; Wallacher, D.; Ramsteiner, M.; Mogilatenko, A.; Rademann, K.; Fischer, S. F. Controlled Pore Formation on Mesoporous Single Crystalline Silicon Nanowires: Threshold and Mechanisms. *J. Nanomater.* **2015**, *2015*, No. 672305.
(45) Prehal, C.; Koczwara, C.; Amenitsch, H.; Presser, V.; Paris, O. Salt concentration and charging velocity determine ion charge storage mechanism in nanoporous supercapacitors. *Nat. Commun.* **2018**, *9*, No. 4145.
(46) Prehal, C.; Koczwara, C.; Jäckel, N.; Schreiber, A.; Burian, M.; Amenitsch, H.; Hartmann, M.; Presser, V.; Paris, O. Quantification of ion confinement and desolvation in nanoporous carbon supercapacitors with modelling and in situ X-ray scattering. *Nat. Energy* **2017**, *2*, No. 16215.
(47) Jäckel, N.; Simon, P.; Gogotsi, Y.; Presser, V. Increase in Capacitance by Subnanometer Pores in Carbon. *ACS Energy Lett.* **2016**, *1*, 1262−1265.
(48) Zheng, C.; Zhou, X.; Cao, H.; Wang, G.; Liu, Z. Synthesis of porous graphene/activated carbon composite with high packing density and large specific surface area for supercapacitor electrode material. *J. Power Sources* **2014**, *258*, 290−296.
(49) Li, H.; Pan, L.; Nie, C.; Liu, Y.; Sun, Z. Reduced graphene oxide and activated carbon composites for capacitive deionization. *J. Mater. Chem.* **2012**, *22*, 15556−15561.
(50) Abbas, Q.; Ratajczak, P.; Babuchowska, P.; Comte, A. L.; Bélanger, D.; Brousse, T.; Béguin, F. Strategies to Improve the Performance of Carbon/Carbon Capacitors in Salt Aqueous Electrolytes. *J. Electrochem. Soc.* **2015**, *162*, A5148−A5157.
(51) Zhang, S.; Pan, N. Supercapacitors Performance Evaluation. *Adv. Energy Mater.* **2015**, *5*, No. 1401401.
(52) Mathis, T.; Kurra, N.; Wang, X.; Pinto, D.; Simon, P.; Gogotsi, Y. Energy Storage Data Reporting in Perspective—Guidelines for Interpreting the Performance of Electrochemical Energy Storage Systems. *Adv. Energy Mater.* **2019**, *9*, No. 1902007.
(53) Dsoke, S.; Tian, X.; Täubert, C.; Schlüter, S.; Wohlfahrt-Mehrens, M. Strategies to reduce the resistance sources on Electrochemical Double Layer Capacitor electrodes. *J. Power Sources* **2013**, *238*, 422−429.

https://dx.doi.org/10.1021/acsaem.0c02908
ACS Appl. Energy Mater. 2021, 4, 1763−1773

(54) Masarapu, C.; Zeng, H.; Hung, K.; Wei, B. Effect of temperature on the capacitance of carbon nanotube supercapacitors. *ACS Nano* **2009**, *3*, 2199−2206.
(55) Taberna, P. L.; Simon, P.; Fauvarque, J. F. Electrochemical Characteristics and Impedance Spectroscopy Studies of Carbon-Carbon Supercapacitors. *J. Electrochem. Soc.* **2003**, *150*, A292−A300.
(56) Lee, H.-M.; Kim, K.; Park, Y.; An, K.; Park, S.; Kim, B. Activated carbons from thermoplastic precursors and their energy storage applications. *Nanomaterials* **2019**, *9*, 896.
(57) Guo, S.; Wang, F.; Chen, H.; Ren, H.; Wang, R.; Pan, X. Preparation and performance of polyvinyl alcohol-based activated carbon as electrode material in both aqueous and organic electrolytes. *J. Solid State Electrochem.* **2012**, *16*, 3355−3362.
(58) Abdulhakeem, B.; Farshad, B.; Damilola, M.; Fatemeh, T.; Mopeli, F.; Julien, D.; Ncholu, M. Morphological characterization and impedance spectroscopy study of porous 3D carbons based on graphene foam-PVA/phenol-formaldehyde resin composite as an electrode material for supercapacitors. *RSC Adv.* **2014**, *4*, 39066−39072.
(59) Liu, M.; Yu, Y.; Liu, B.; Liu, L.; Lv, H.; Chen, A. PVP-assisted synthesis of nitrogen-doped hollow carbon spheres for supercapacitors. *J. Alloys Compd.* **2018**, *768*, 42−48.
(60) Ma, C.; Li, Z.; Li, J.; Fan, Q.; Wu, L.; Shi, J.; Song, Y. Lignin-based hierarchical porous carbon nanofiber films with superior performance in supercapacitors. *Appl. Surf. Sci.,* **2018**, *456*, 568−576.
(61) Zhang, W.; Yu, C.; Chang, L.; Zhong, W.; Yang, W. Three-dimensional nitrogen-doped hierarchical porous carbon derived from cross-linked lignin derivatives for high performance supercapacitors. *Electrochim. Acta* **2018**, *282*, 642−652.
(62) Tong, Y.-X.; Li, X-M.; Xie, L-J.; Su, F-Y.; Li, J-P.; Sun, G-H.; Gao, Y-D.; Zhang, N.; Wei, Q.; Chen, C-M. Nitrogen-doped hierarchical porous carbon derived from block copolymer for supercapacitor. *Energy Storage Mater.* **2016**, *3*, 140−148.
(63) Wang, Y.; Bin Kong, L.; Li, X.; Ran, F.; Luo, Y.; Kang, L. Mesoporous carbons for supercapacitors obtained by the pyrolysis of block copolymers. *New Carbon Mater.* **2015**, *30*, 302−309.
(64) Chen, G.; Zhai, W.; Wang, Z.; Yu, J.; Wang, F.; Zhao, Y.; Li, G. Fabrication and supercapacitive properties of hierarchical porous carbon from polyacrylonitrile. *Mater. Res. Bull.* **2015**, *72*, 204−210.
(65) Yadav, N.; Ritu; Promila; Hashmi, S. A. Hierarchical porous carbon derived from eucalyptus-bark as a sustainable electrode for high-performance solid-state supercapacitors. *Sustainable Energy Fuels* **2020**, *4*, 1730−1746.
(66) Demir, M.; Saraswat, S.; Gupta, R. Hierarchical nitrogen-doped porous carbon derived from lecithin for high-performance supercapacitors. *RSC Adv.* **2017**, *7*, 42430−42442.
(67) Laheäär, A.; Przygocki, P.; Abbas, Q.; Béguin, F. Appropriate methods for evaluating the efficiency and capacitive behavior of different types of supercapacitors. *Electrochem. Commun.* **2015**, *60*, 21−25.

https://dx.doi.org/10.1021/acsaem.0c02908
ACS Appl. Energy Mater. 2021, 4, 1763−1773